

# Simultaneous functional photoacoustic and ultrasonic endoscopy of internal organs *in vivo*

Joon-Mo Yang<sup>1</sup>, Christopher Favazza<sup>1</sup>, Ruimin Chen<sup>2</sup>, Junjie Yao<sup>1</sup>, Xin Cai<sup>1</sup>, Konstantin Maslov<sup>1</sup>, Qifa Zhou<sup>2</sup>, K Kirk Shung<sup>2</sup> & Lihong V Wang<sup>1</sup>

**At present, clinicians routinely apply ultrasound endoscopy in a variety of interventional procedures that provide treatment solutions for diseased organs. Ultrasound endoscopy not only produces high-resolution images, but also is safe for clinical use and broadly applicable. However, for soft tissue imaging, its mechanical wave-based image contrast fundamentally limits its ability to provide physiologically specific functional information. By contrast, photoacoustic endoscopy possesses a unique combination of functional optical contrast and high spatial resolution at clinically relevant depths, ideal for imaging soft tissues. With these attributes, photoacoustic endoscopy can overcome the current limitations of ultrasound endoscopy. Moreover, the benefits of photoacoustic imaging do not come at the expense of existing ultrasound functions; photoacoustic endoscopy systems are inherently compatible with ultrasound imaging, thereby enabling multimodality imaging with complementary contrast. Here we present simultaneous photoacoustic and ultrasonic dual-mode endoscopy and show its ability to image internal organs *in vivo*, thus illustrating its potential clinical application.**

Endoscopic ultrasound (EUS)<sup>1,2</sup> is currently the most clinically translated tomographic endoscopic imaging modality, and it has made key contributions to medicine by enabling new interventional procedures in many medical areas, such as gastroenterology<sup>1,3–6</sup>, pulmonology<sup>1,7,8</sup> and urology<sup>1,9,10</sup>. Representative applications<sup>1,2</sup> of this technique include EUS-guided sample collection from disease-affected tissue (so-called fine needle aspiration); tissue ablation or endosurgery; interventional device deployment or implantation; and oncologic treatments, such as fine needle injection of chemotherapeutic drugs. Compared with other mainstream medical imaging modalities, such as magnetic resonance imaging, X-ray computed tomography and positron emission tomography, ultrasound imaging is easily embodied in an endoscopic probe, uses extremely safe mechanical waves and permits bedside operation. Moreover, it provides high-speed, high-resolution, cross-sectional imaging over a large field of view (FOV).

Lung, colorectal, pancreatic and prostate cancer are leading causes of cancer mortality<sup>11</sup>, and all these cancers are located in or close to

the respiratory system or gastrointestinal tract, in which endoscopic procedures are applicable. Although EUS-based imaging studies have shown the ability to diagnose these cancers<sup>1,3–10</sup>, most of the current applications of EUS are primarily focused on guiding other interventional procedures<sup>1,2</sup>. Early-stage tumor detection or *in situ* characterization of diseased tissues is challenging for EUS because its contrast mechanism relies on bulk mechanical properties. Tumor boundaries and connections with surrounding blood or lymphatic vessels are clinically relevant and provide necessary information for assessing disease stage or progress<sup>12</sup> and planning treatment therapies. However, pure ultrasound-based image contrast does not sufficiently provide this crucial information. Recently developed optical endoscopic imaging modalities, such as endoscopic optical coherence tomography<sup>13–15</sup>, confocal endoscopy<sup>16</sup> and endoscopic polarized scanning spectroscopy<sup>17,18</sup>, can detect diseased tissues and abnormal tissue changes, such as dysplasia, with high sensitivity and high spatial resolution. Still, these techniques are limited by their inability to image targets beyond a ~1–2 mm depth because of the strong optical scattering properties of tissue.

Photoacoustic tomography (PAT) is a new imaging modality that can provide volumetric images of biological tissues *in vivo* with high spatial resolution at depths<sup>19–21</sup> that far exceed the penetration depths of conventional high-resolution optical imaging modalities<sup>13–18</sup>. PAT systems are very similar to ultrasound imaging systems because they both use ultrasound detection to render an image; however, PAT produces images with optical absorption-based contrast. By using deeply penetrable diffused light to excite photoacoustic signals, PAT can image targets several centimeters deep in soft tissues<sup>21</sup>. With high optical contrast, tumor boundaries and surrounding lymphovascular systems can be resolved with endogenous or exogenous contrast agents<sup>22–26</sup>. Additionally, other types of physiological or functional information, including total hemoglobin concentration, oxygen saturation of hemoglobin (sO<sub>2</sub>)<sup>22</sup>, blood flow<sup>27</sup> or temperature<sup>28,29</sup>, are also measurable. Therefore, photoacoustic endoscopy (PAE)<sup>30</sup> that embodies PAT in a small probe can be used as a new, minimally invasive diagnostic tool for providing optical absorption-based contrast with high spatial resolution while maintaining the capabilities and benefits of traditional EUS. Here we report what is, to our knowledge,

<sup>1</sup>Optical Imaging Laboratory, Department of Biomedical Engineering, Washington University in St. Louis, St. Louis, Missouri, USA. <sup>2</sup>Department of Biomedical Engineering, National Institutes of Health Ultrasonic Transducer Resource Center, University of Southern California, Los Angeles, California, USA. Correspondence should be addressed to L.V.W. (lhwang@biomed.wustl.edu) for the system or to Q.Z. (qifazhou@usc.edu) for the ultrasonic transducers.

Received 22 March 2011; accepted 18 November 2011; published online 15 July 2012; doi:10.1038/nm.2823

the first *in vivo* demonstrations of simultaneous PAE and EUS imaging in the upper and lower gastrointestinal tracts of animals with our new integrated endoscopic system.

RESULTS

We developed an integrated PAE and EUS imaging system for simultaneous, photoacoustic and ultrasonic imaging of internal organs *in vivo* (Fig. 1, Supplementary Figs. 1 and 2 and Supplementary Video 1). The ultrasonic images are produced with conventional pulse-echo imaging that detects acoustic waves reflected from target tissue; the photoacoustic images are formed through detection of acoustic waves generated by rapid thermoelastic expansion caused by optical absorption of short laser pulses<sup>21</sup>. A focused ultrasonic transducer detects one-dimensional depth-resolved signals (or A-lines), and cross-sectional images (or B-scans) are produced by rotating a scanning mirror that directs both optical and acoustic waves. The endoscope system records and displays a set of dual wavelength photoacoustic and ultrasonic B-scan images in real time during the constant rotation (~4 Hz) of the mirror. By interleaving two optical pulses of different wavelengths and one acoustic pulse at each angular step of the mirror, spatially coincident images are recorded from the generated photoacoustic and ultrasonic A-line signals, even during periods of substantial motion of the target. Volumetric data sets are acquired by recording sequential A-line data during the constant rotational motion of the mirror and mechanical pullback of the probe at a speed of ~200 μm s<sup>-1</sup>. Oxy- and deoxyhemoglobins, two of the dominant absorbers of visible light in most soft biological tissue, have different absorption spectra. With dual-wavelength photoacoustic imaging, it is possible to calculate total hemoglobin concentration and sO<sub>2</sub> values (Supplementary Fig. 3)<sup>20,24</sup>.

Upper gastrointestinal tract imaging *in vivo*

We imaged the esophagi of four adult New Zealand white rabbits (Supplementary Fig. 4) and collected 5–10 volumetric data sets from each rabbit without complications. We recorded about 2,800 B-scan slices at ~50-μm intervals for each volumetric set of PAT at 562 nm, PAT at 584 nm and ultrasonic imaging. The endoscopic system provides anatomic information of the rabbit's esophagus, surrounding tissue and proximal organs, covering an approximately 14-cm-long,

18-mm-diameter volume (Fig. 2 and Supplementary Video 2) within a scanning time of ~12 min. Volume renderings enable three-dimensional (3D) visualization of the morphology and configuration of organs surrounding the esophagus with both contrast mechanisms (Fig. 2a–c and Supplementary Video 3). We created the photoacoustic image (Fig. 2a) from data acquired at a 584-nm laser wavelength in which the photoacoustic signal is proportional to the total hemoglobin concentration. Both the photoacoustic (Fig. 2a) and ultrasonic (Fig. 2b) images show the lung and trachea profiles where they abut the esophagus; however, only the photoacoustic image (Fig. 2a) provides peripheral vasculature information of these organs. Through transesophageal imaging, the tomographic endoscope obtained cross-sectional images of the lung with optical absorption-based contrast (Fig. 2d) and acoustic reflectance-based contrast (Fig. 2e). We found obvious differences in the locations of the contrast origins for the two imaging modes (Fig. 2f). When the endoscope passed by the trachea, we observed strong photoacoustic (Fig. 2g) and ultrasonic (Fig. 2h) signals around the contact point between the esophagus and trachea, which run parallel (Fig. 2i) from the cricoid cartilage to the carina. The probe's limited angular FOV covers only ~270°. To obtain a full 360° view, we reinserted the probe with 180° rotation and imaged the dorsal region of the esophagus. These results are shown in Supplementary Figure 5 and Supplementary Video 4.

For a straightforward comparison of the volumetric images over the entire 360° view, we combined the ventral (Fig. 2) and dorsal (Supplementary Fig. 5) volumetric data sets, using the method described in Supplementary Figure 6, and produced three radial-maximum amplitude projection (RMAP) images, which show the total hemoglobin distribution (Fig. 3a), the sO<sub>2</sub> level (Fig. 3b) and the ultrasonic echogenicity distribution (Fig. 3c), respectively. To produce the sO<sub>2</sub> distribution over the scanned area (Fig. 3b), we spectrally analyzed dual-wavelength photoacoustic data sets (Supplementary Fig. 3). The 584-nm photoacoustic image (Fig. 3a) shows the total hemoglobin distribution in the lung, trachea and surrounding blood vessels. Also, the aorta and caudal vena cava are shown in the image (Fig. 3a) and are distinguished from each other by differences in sO<sub>2</sub> (Fig. 3b). As confirmed by dissection after imaging (Supplementary Fig. 7), the heart was located near the mid-ventral line between the two lobes of the lung, and several prominent blood

**Figure 1** Illustration of simultaneous, multiwavelength photoacoustic (PA) and ultrasonic (US) endoscopy. (a) The endoscope carries out circumferential sector scanning by rotating a scanning mirror, which reflects both the ultrasonic waves and laser pulses and enables static mounting of the associated illumination and ultrasonic pulse-generation detection units. At each angular step of the mirror (~1.42°), both the first (λ<sub>1</sub>) and second (λ<sub>2</sub>) pulsed laser beams are independently fired through the optical fiber and the acoustic pulse is generated by the ultrasonic transducer with a constant time delay of ~30 μs between each of the laser and acoustic pulses. The ensuing photoacoustic and ultrasonic echo waves are detected and converted into electric signals by the ultrasonic transducer; the signals are then recorded and displayed on a computer. The 30-μs time delay is necessary to ensure that the sample has relaxed and that consecutive signals will not interfere with each other. However, this delay does not substantially affect co-registration of the three images because the difference between the angular positions of each signal is small and is well within the spatial resolution of the detector. (b) A photo shows the side-scanning 3.8-mm-diameter probe prototype firing a 562-nm laser beam. Scale bar, 2 cm. (c) Definition of Cartesian and cylindrical coordinate systems. The +z axis is defined along the endoscope axis (or pullback direction). (d) A volumetric image comprising consecutive B-scan slices. (e) A representative cross-section of d along the x-y plane, which shows the endoscope's 270° angular FOV.

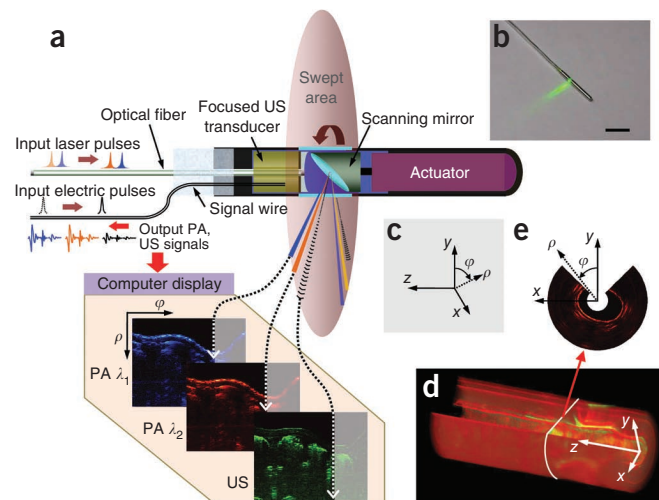
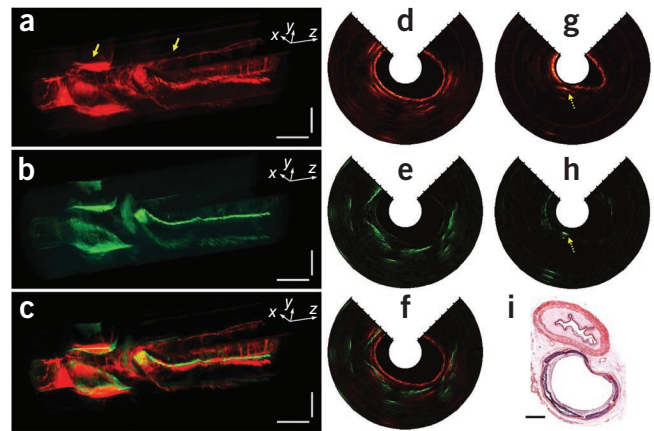


**Figure 2** Simultaneous, co-registered, PAE-EUS pseudocolor images from a rabbit esophagus *in vivo*. (a) Three-dimensionally rendered photoacoustic structural image. The left- and right-hand sides of this image correspond to the lower and upper esophagus, respectively, and the lower portion ( $-y$  axis) to the ventral side of the rabbit. To more clearly show the structures surrounding the esophagus, we excluded signals generated from the esophagus. (b) Co-registered ultrasonic structural image for the same volume of a. (c) An overlaid image of a and b. In a–c, the horizontal and vertical scale bars represent 2 cm and 5 mm, respectively. (d) A representative photoacoustic  $x$ - $y$  cross-sectional image (18 mm in diameter) near the lung, as indicated by the left arrow in a. The  $\sim 0.8$ -mm-thick region from the inner surface of the imaged lumen represents the signals from the esophagus. The surface of the lung is shown  $\sim 1$  mm from the inner surface. (e) Corresponding ultrasonic cross-sectional image of d. (f) A combined image of d and e. (g) A representative photoacoustic  $x$ - $y$  cross-sectional image (18 mm in diameter) near the trachea, as indicated by the right arrow in a. (h) Corresponding ultrasonic cross-sectional image of g. In g and h, the dotted arrows indicate the contact point between the trachea and the esophagus. In d–h, the hash marks represent 1-mm intervals. (i) Representative histology (H&E stain) of the esophagus (top) and trachea (bottom). Scale bar, 1 mm.



vessels (see the arrow in Fig. 3a), including the aorta and caudal vena cava, branched out from the heart. The aorta and caudal vena cava show reasonable  $sO_2$  values of  $\sim 95\%$  and  $\sim 70\%$ , respectively (Fig. 3b). The adventitial surface of the trachea and the network of the prominent blood vessels distributed in the apical lung pleura (Fig. 3b) show relatively high  $sO_2$  because they directly receive fully oxygenated blood from the heart. Strong ultrasonic contrast was generated at the lung's surface and the trachea (Fig. 3c), which contains cartilage (Fig. 2i). The image reproducibility of the endoscope is presented in Supplementary Figure 8.

**Lower gastrointestinal tract and lymphatic system imaging *in vivo***

We imaged the lower gastrointestinal tracts of Sprague-Dawley rats using the same scanning parameters (Supplementary Fig. 9). Within a scanning time of  $\sim 4.6$  min, we imaged the descending colon of a rat over a section  $\sim 5.5$  cm in length and  $\sim 12$  mm in diameter. Volumetric images clearly show the lumen's architecture (Fig. 4a and Supplementary Video 5). Photoacoustic imaging shows densely distributed blood vasculature in the colon wall, whereas ultrasonic

imaging shows the density of tissue in the mucosal and submucosal layers and other mesenteric tissues entangled around the tract (Fig. 4a). Compared with single-mode EUS<sup>1,6</sup>, PAE-EUS provides high-resolution vasculature information in the gastrointestinal tract and clearly shows optical and mechanical contrast differences. The corresponding  $sO_2$  map (Fig. 4b) shows the oxygen saturation variation in the imaged blood vessels. The ultrasonic RMAP image (Fig. 4c) shows hyperechoic regions generated by the lumen wall and exterior tissues. The photoacoustic images also show strong signals from blood vessels; however, corresponding ultrasonic signals are very weak at those locations (Fig. 4d,e). Although the ultrasonic imaging provided an approximate boundary profile of the colon, its overall contrast is weak owing to the low echogenicity of the soft mucosal tissues (Fig. 4f).

To demonstrate lymphangiographic imaging, we imaged parts of the lymphatic system near the lower gastrointestinal tracts in Sprague-Dawley rats (Supplementary Fig. 10). Accumulation of Evans blue dye provided the photoacoustic image contrast for the lymph nodes and vessels, which are not intrinsically optically absorptive in the visible spectrum. We targeted lymph nodes near the dorsal zone of the descending colon. In these experiments, we used 523-nm light to image the surrounding blood vasculature and 640-nm light to image the accumulation of Evans blue in the lymphatic system, which has an absorption peak at  $\sim 610$  nm (Supplementary Fig. 3). After recording a set of control images, we injected  $\sim 0.4$  ml of Evans blue dye (0.3%) in the inner legs of the rats, and then acquired serial volumetric

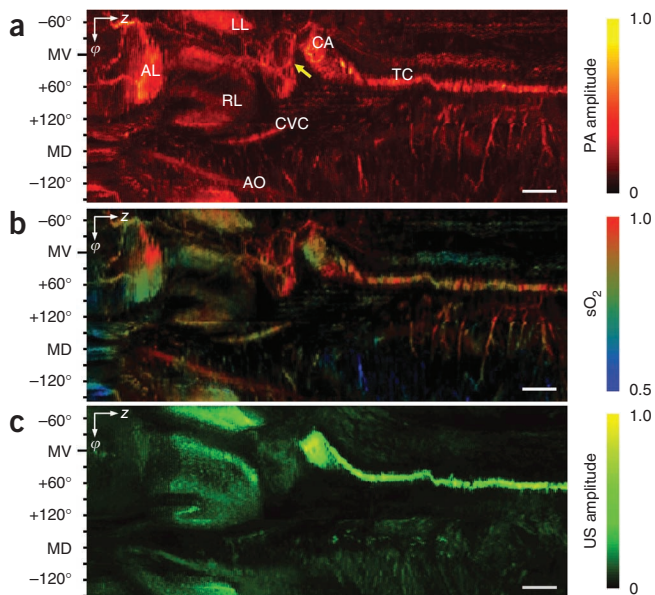
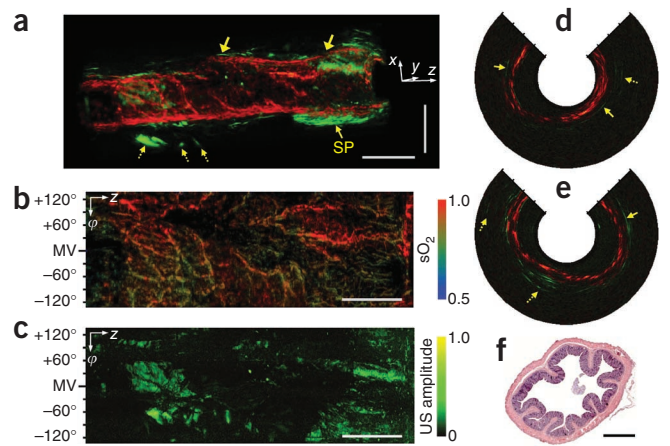


**Figure 3** RMAP images over a full 360° angular FOV (views from the inside of the esophagus). The left- and right-hand sides of these three images correspond to the lower and upper esophagus, respectively. (a) Normalized photoacoustic RMAP image showing the total hemoglobin distribution, with the esophageal signals excluded during the RMAP construction. AL, accessory lobe; LL, left lobe; RL, right lobe of the lung; AO, aorta; CVC, caudal vena cava; CA, carina; TC, trachea. (b) Functional photoacoustic RMAP image showing the  $sO_2$  levels of the imaged structures in a. (c) Normalized ultrasonic RMAP image showing the echogenicity distribution. In each image, the vertical  $\phi$  axis corresponds to the angular range of 360°, and the horizontal  $z$  axis corresponds to the pullback length of 14 cm. The approximate mid-ventral (MV) position and angular measures from the MV position are marked along the vertical  $\phi$  axis; the positive and negative values correspond to the right and left sides of the animal and MD denotes the mid-dorsal position. Scale bars, 1 cm (for the horizontal direction only).



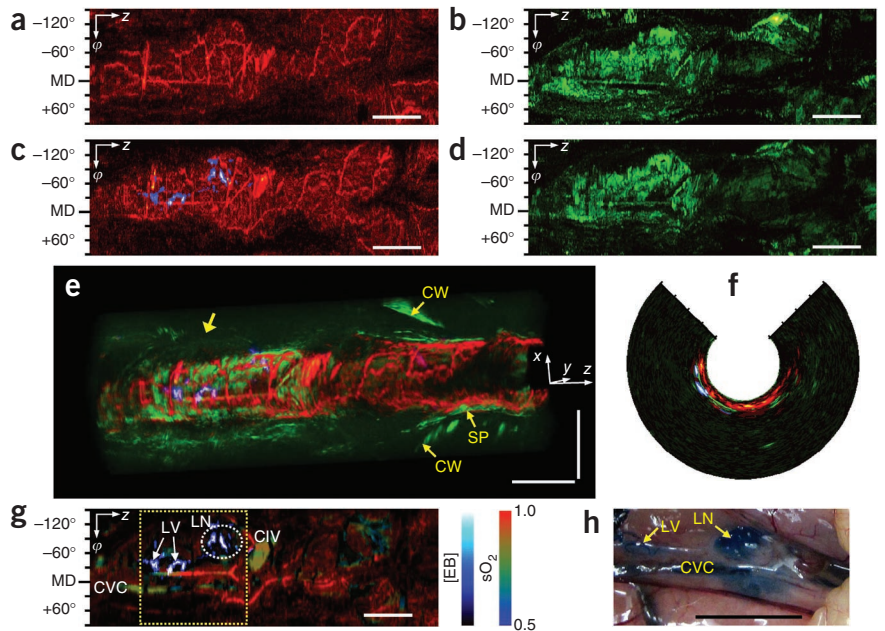
**Figure 4** Simultaneous, co-registered, PAE-EUS colonoscopic pseudocolor images of a rat colon acquired *in vivo*. (a) Three-dimensionally rendered photoacoustic-ultrasonic structural image. The right side of this image is closer to the anus, and the negative  $y$  axis corresponds to the ventral direction of the animal. The red and green colors correspond to photoacoustic and ultrasonic signals, respectively. The dotted arrows indicate mesenteric tissue entangled around the tract, and SP denotes the sphincter. Scale bars, 1 cm (horizontal) and 5 mm (vertical). (b) Photoacoustic RMAP image showing the  $sO_2$  levels of the imaged structures in a (views from the inside of the colon). (c) Corresponding (to b) ultrasonic RMAP image showing the echogenicity distribution. In b and c, the vertical  $\phi$  axis corresponds to the angular FOV covering  $270^\circ$ , and the horizontal  $z$  axis corresponds to the pullback length of 5.5 cm. The approximate mid-ventral (MV) position and angular measures from the MV position are marked along the vertical  $\phi$  axis, where the positive and negative values correspond to the right and left sides of the rat. Scale bars, 1 cm (for the horizontal direction only). (d,e) Photoacoustic-ultrasonic cross-sectional images from the position indicated by the left and right arrows in a, respectively. In d and e, the solid arrows indicate the outer boundary of the colon, and mesenteric tissues are marked with dotted arrows. The hash marks represent 1-mm intervals. (f) A typical histology image (H&E stain) of the colon. Scale bar, 1 mm.



data sets every 20 min for  $\sim 1$  h (Supplementary Fig. 11). In each instance, we imaged a volume of  $\sim 7.2$  cm in length and 12 mm in diameter, with a scanning time of  $\sim 8$  min. Serial photoacoustic RMAP images acquired at 640 nm showed an obvious photoacoustic signal increase and dynamic changes of the Evans blue distribution in the lymphatic system, and spectroscopic analysis at the two wavelengths enabled accurate differentiation between the blood and lymph signals (Supplementary Fig. 11). We present a set of photoacoustic and ultrasonic images containing both pre- (Fig. 5a,b) and postcontrast injection images (Fig. 5c,d), which illustrates the capability of contrast-enhanced photoacoustic imaging of the local lymphatic system. We observed the strongest Evans blue signals in the photoacoustic RMAP image (Fig. 5c) acquired  $\sim 40$  min after Evans blue injection; they are clearly different from those in the control photoacoustic RMAP image

(Fig. 5a). However, the corresponding ultrasonic image (Fig. 5d) did not show any notable changes from the control image (Fig. 5b). Volume rendering of the co-registered dual-wavelength photoacoustic and ultrasonic signals enables 3D visualization of the lymphovascular structure (PAE) inside a density map (EUS) of the tissue (Fig. 5e, Supplementary Videos 6 and 7). As shown in a cross-sectional image (Fig. 5f), the lymph nodes are in contact with the outer colon wall. A spectrally processed photoacoustic RMAP image (Fig. 5g), which excludes signal from the colon, clearly shows the  $sO_2$  distribution and lymph structures in the imaged anatomy outside the colon and provides an effective comparison with the surgical photo (Fig. 5h and Supplementary Fig. 12). Notably, PAE detected signals from lymph vessels as small as  $\sim 1$  mm in diameter, far exceeding the current capabilities of EUS<sup>1,5,7,8</sup>.

**Figure 5** Lymphovascular system imaging *in vivo* near a rat colon. (a) Control photoacoustic RMAP image before Evans blue (EB) administration (views from the inside of the colon). The right side of this image is closer to the anus. (b) Co-registered ultrasonic RMAP image of a. (c) Photoacoustic RMAP image at  $\sim 40$  min after injection (processed from the dual-wavelength data). The red and blue colors represent photoacoustic signals from blood and Evans blue, respectively. (d) Corresponding ultrasonic RMAP image of c. In a–d, the vertical  $\phi$  axis corresponds to the angular FOV covering  $270^\circ$ , and the horizontal  $z$  axis corresponds to the pullback length of 7.2 cm. The approximate mid-dorsal (MD) position and angular measures from the MD position are marked along the vertical  $\phi$  axis. (e) Merged volumetric image of c and d. SP, sphincter; CW, cavity wall. (f) A representative  $x$ - $y$  cut near the location indicated by the arrow in e. The blue-colored regions represent a lymph node. (g) A spectrally processed photoacoustic RMAP image from the data set shown in c, with the colon signals excluded. This image shows the lymph structures and  $sO_2$  distribution of the surround vasculature outside the colon. The arrows indicate lymph vessels (LV), and the dotted circle corresponds to the left lumbar node (LN) in h. CVC, caudal vena cava; CIV, left common iliac vein. (h) A postimaging surgical photo showing the stained lymph node and vessels located outside the colon. This area approximately corresponds to the yellow dotted square in g. Scale bars, 1 cm (horizontal) and 5 mm (vertical).



## DISCUSSION

PAE's unique combination of optical absorption contrast, wide FOV and great penetration depth suggests many possibilities for medical applications involving diagnostic or interventional procedures. Most notably, PAE can be realized simply through a few modifications and the addition of a light-delivery system to EUS technology while conserving EUS capabilities. The simultaneous, spatially coincident photoacoustic and ultrasonic dual-mode imaging provides unprecedented information and promotes morphologic and functional understanding of the target tissue. In the upper gastrointestinal tract images (Fig. 2), we observed organs surrounding the esophagus, such as the lung and trachea, in both the photoacoustic and ultrasonic images; however, only photoacoustic images showed their adjacent vasculatures. Although contrast-enhanced ultrasonic techniques<sup>1,9,10</sup> such as Doppler ultrasound<sup>1,31</sup> are capable of imaging blood vessels, these techniques' sensitivities are all much lower than that of PAT, which has recently achieved sufficient signal sensitivity to detect single red blood cells<sup>32</sup>. Additionally, photoacoustic imaging provides functional information with endogenous contrast (Figs. 2–4), and, with the aid of an exogenous contrast agent, it can also provide information about the dynamics of regional lymph systems (Fig. 5 and Supplementary Fig. 11). These experimental results show the dual-mode endoscope's transenteric deep imaging ability and its complementary contrast production.

PAE signal detection is predicated on the same basic principles as EUS signal detection, and the required components for light delivery do not substantially affect the probe's endoscopic functionality. Therefore, this integrated endoscopic technique could be translated into virtually all current application areas of EUS<sup>1,2</sup>. Added angiographic and spectral imaging functions would enhance EUS's role in addressing the aforementioned high-mortality cancers and in many other clinical applications. From diagnosis to therapy, the possible contributions of PAE are conceived as follows. First, PAE's strong spectroscopic imaging ability and high optical contrast could promote incidental findings of disease symptoms in many routine endoscopic procedures. Tumor detection with conventional single-mode EUS has been a challenge because of the similar mechanical properties between diseased and healthy soft tissue, as well as between blood and lymph vessels. PAE's spectral imaging ability, based on physiologically-specific endogenous optical contrasts, yields vital functional information, which might enable earlier detection of tissue abnormalities. Additionally, on the basis of the lymphovascular information that PAE can provide, it might improve the accuracy of cancer staging. Contrast agents for EUS are limited, whereas PAE's unique broad-spectrum, absorption-based contrast fosters the use of various kinds of contrast agents<sup>24–26</sup>, thus enabling many applications, such as lymph node mapping<sup>23,26</sup> and molecular imaging for cancer mapping and staging<sup>12,24,25,33</sup>. Finally, PAE's high contrast and high resolution vasculature imaging ability could enable more advanced interventional procedures by helping practitioners guide devices to extract samples for biopsy or to inject drugs for chemotherapy.

Another key feature of PAT is its exceptional scalability<sup>21</sup>, spanning from providing subcellular resolution at shallow depths to providing optical contrast of tissue several centimeters deep with ultrasound-level spatial resolution. For lumen wall imaging in which great penetration depth is not necessary, optically resolved photoacoustic imaging could provide greater spatial resolution<sup>32</sup>. In many clinical transenteric imaging applications, deep imaging ability is preferable to shallow high-spatial-resolution imaging. By choosing a lower-center-frequency transducer, red-shifting laser wavelengths to the

near-infrared spectrum or increasing the laser pulse energy by enlarging the illumination area, the penetration depth of PAE can be greatly improved, thus making it more applicable to current clinical requirements (see **Supplementary Discussion**). In this study, we used a pair of laser beams at 584 nm and 562 nm to determine the distributions of total hemoglobin concentration and sO<sub>2</sub>, and we used another pair at 640 nm and 523 nm to image the lymphovascular system with the aid of a contrast agent. However, one can freely choose illumination wavelengths, from ultraviolet to near-infrared, to quantitatively evaluate other cellular or physiological constituents, such as cell nuclei<sup>34</sup> or hydration levels<sup>35</sup>. Further, more laser pulses can be added to each angular step of the mirror to generate richer spectral information for a thorough characterization of diseased tissues. With the integration of PAE, EUS could become a powerful clinical tool.

## METHODS

Methods and any associated references are available in the online version of the paper.

*Note: Supplementary information is available in the online version of the paper.*

## ACKNOWLEDGMENTS

We thank J. Ballard for his attentive reading of the manuscript. We also thank J. Kalishman, P. Jiménez-Bluhm, and L. Andrews-Kaminsky for helping with animal preparation, surgery, and image interpretation. We thank B. Matthews, V. Tsytsarev, G. Lanza, R. Senior, and J. Atkinson for helpful discussion on the experimental results. This work was sponsored in part by US National Institutes of Health grants R01 CA157277, R01 EB000712, R01 EB008085, R01 CA134539, P41-EB2182, and U54 CA136398 (Network for Translational Research). J.-M.Y. was supported in part by a Korea Research Foundation Grant funded by the Korean government (KRF-2007-357-C00039).

## AUTHOR CONTRIBUTIONS

J.-M.Y. built the system, did the experiments, and wrote the manuscript. C.F. developed the data acquisition program, carried out the experiments, and co-wrote the manuscript. R.C., Q.Z., and K.K.S. designed and fabricated the ultrasonic transducers. J.Y. contributed to the data processing algorithms and also assisted with data processing and experiments. X.C. helped with the experiments. K.M. contributed to the system development. L.V.W. directed the project, conceived the endoscope design, discussed the experiments and revised the manuscript.

## COMPETING FINANCIAL INTERESTS

The authors declare competing financial interests: details are available at <http://www.nature.com/doi/10.1038/nm.2823>.

Published online at <http://www.nature.com/doi/10.1038/nm.2823>.

Reprints and permissions information is available online at <http://www.nature.com/reprints/index.html>.

- Dietrich, C. *Endoscopic Ultrasound: An Introductory Manual and Atlas*, (Thieme, New York, 2006).
- Kaul, V. *et al.* Interventional EUS. *Gastrointest. Endosc.* **72**, 1–4 (2010).
- Rösch, T. *et al.* Localization of pancreatic endocrine tumors by endoscopic ultrasonography. *N. Engl. J. Med.* **326**, 1721–1726 (1992).
- Gress, F.G., Hawes, R.H., Savides, T.J., Ikenberry, S.O. & Lehman, G.A. Endoscopic ultrasound-guided fine-needle aspiration biopsy using linear array and radial scanning endosonography. *Gastrointest. Endosc.* **45**, 243–250 (1997).
- Chang, K.J., Nguyen, P., Erickson, R.A., Durbin, T.E. & Katz, K.D. The clinical utility of endoscopic ultrasound-guided fine-needle aspiration in the diagnosis and staging of pancreatic carcinoma. *Gastrointest. Endosc.* **45**, 387–393 (1997).
- Fu, K.I. *et al.* Staging of early colorectal cancers: magnifying colonoscopy versus endoscopic ultrasonography for estimation of depth of invasion. *Dig. Dis. Sci.* **53**, 1886–1892 (2008).
- Silvestri, G.A. *et al.* Endoscopic ultrasound with fine-needle aspiration in the diagnosis and staging of lung cancer. *Ann. Thorac. Surg.* **61**, 1441–1445, discussion 1445–1446 (1996).
- Navani, N., Spiro, S.G. & Janes, S.M. Mediastinal staging of NSCLC with endoscopic and endobronchial ultrasound. *Nat. Rev. Clin. Oncol.* **6**, 278–286 (2009).
- Salomon, G. *et al.* Evaluation of prostate cancer detection with ultrasound real-time elastography: a comparison with step section pathological analysis after radical prostatectomy. *Eur. Urol.* **54**, 1354–1362 (2008).

10. Trabulsi, E.J., Sackett, D., Gomella, L.G. & Halpern, E.J. Enhanced transrectal ultrasound modalities in the diagnosis of prostate cancer. *Urology* **76**, 1025–1033 (2010).
11. Jemal, A., Siegel, R., Xu, J. & Ward, E. Cancer statistics, 2010. *CA Cancer J. Clin.* **60**, 277–300 (2010).
12. Steeg, P.S. Tumor metastasis: mechanistic insights and clinical challenges. *Nat. Med.* **12**, 895–904 (2006).
13. Tearney, G.J. *et al.* *In vivo* endoscopic optical biopsy with optical coherence tomography. *Science* **276**, 2037–2039 (1997).
14. Yun, S.H. *et al.* Comprehensive volumetric optical microscopy *in vivo*. *Nat. Med.* **12**, 1429–1433 (2006).
15. Adler, D.C. *et al.* Three-dimensional endomicroscopy using optical coherence tomography. *Nat. Photonics* **1**, 709–716 (2007).
16. Kiesslich, R. *et al.* Confocal laser endoscopy for diagnosing intraepithelial neoplasias and colorectal cancer *in vivo*. *Gastroenterology* **127**, 706–713 (2004).
17. Qiu, L. *et al.* Multispectral scanning during endoscopy guides biopsy of dysplasia in Barrett's esophagus. *Nat. Med.* **16**, 603–606 (2010).
18. Terry, N.G. *et al.* Detection of dysplasia in Barrett's esophagus with *in vivo* depth-resolved nuclear morphology measurements. *Gastroenterology* **140**, 42–50 (2011).
19. Oraevsky, A.A. & Karabutov, A.A. Optoacoustic Tomography. in *Biomedical Photonics Handbook*, Vol. PM125 (ed. Vo-Dinh, T.) 3401–3434 (CRC Press, 2003).
20. Wang, L.V. *Photoacoustic Imaging and Spectroscopy* (CRC Press, 2009).
21. Wang, L.V. Multiscale photoacoustic microscopy and computed tomography. *Nat. Photonics* **3**, 503–509 (2009).
22. Zhang, H.F., Maslov, K., Stoica, G. & Wang, L.V. Functional photoacoustic microscopy for high-resolution and noninvasive *in vivo* imaging. *Nat. Biotechnol.* **24**, 848–851 (2006).
23. Erpelding, T.N. *et al.* Sentinel lymph nodes in the rat: noninvasive photoacoustic and US imaging with a clinical US system. *Radiology* **256**, 102–110 (2010).
24. Kim, C., Favazza, C. & Wang, L.V. *In vivo* photoacoustic tomography of chemicals: high-resolution functional and molecular optical imaging at new depths. *Chem. Rev.* **110**, 2756–2782 (2010).
25. De la Zerna, A. *et al.* Carbon nanotubes as photoacoustic molecular imaging agents in living mice. *Nat. Nanotechnol.* **3**, 557–562 (2008).
26. Kim, J.-W., Galanzha, E.I., Shashkov, E.V., Moon, H.-M. & Zharov, V.P. Golden carbon nanotubes as multimodal photoacoustic and photothermal high-contrast molecular agents. *Nat. Nanotechnol.* **4**, 688–694 (2009).
27. Yao, J., Maslov, K.I., Shi, Y., Taber, L.A. & Wang, L.V. *In vivo* photoacoustic imaging of transverse blood flow by using Doppler broadening of bandwidth. *Opt. Lett.* **35**, 1419–1421 (2010).
28. Larina, I.V. *et al.* Real-time photoacoustic monitoring of temperature in tissues. *J. Phys. D Appl. Phys.* **38**, 2633 (2005).
29. Shah, J. *et al.* Photoacoustic imaging and temperature measurement for photothermal cancer therapy. *J. Biomed. Opt.* **13**, 034024 (2008).
30. Yang, J.M. *et al.* Photoacoustic endoscopy. *Opt. Lett.* **34**, 1591–1593 (2009).
31. Xuan, J.W. *et al.* Functional neoangiogenesis imaging of genetically engineered mouse prostate cancer using three-dimensional power Doppler ultrasound. *Cancer Res.* **67**, 2830–2839 (2007).
32. Zhang, C., Maslov, K. & Wang, L.V. Subwavelength-resolution label-free photoacoustic microscopy of optical absorption *in vivo*. *Opt. Lett.* **35**, 3195–3197 (2010).
33. Weissleder, R. & Pittet, M.J. Imaging in the era of molecular oncology. *Nature* **452**, 580–589 (2008).
34. Yao, D.K., Maslov, K., Shung, K.K., Zhou, Q. & Wang, L.V. *In vivo* label-free photoacoustic microscopy of cell nuclei by excitation of DNA and RNA. *Opt. Lett.* **35**, 4139–4141 (2010).
35. Xu, Z., Li, C. & Wang, L.V. Photoacoustic tomography of water in phantoms and tissue. *J. Biomed. Opt.* **15**, 036019 (2010).

## ONLINE METHODS

**Animal experiments.** All procedures in the animal experiments followed the protocols approved by the Institutional Animal Care and Use Committee at Washington University in St. Louis. The animals were housed in a facility at Washington University in St. Louis that is fully accredited by the Association for Assessment and Accreditation of Laboratory Animal Care International. The animals were cared for by a full-time veterinary staff. Before endoscopic imaging, the animals were fasted for ~12 h to reduce the amount of ingesta in the gastrointestinal tracts. After each imaging experiment, the animal was euthanized and subsequently dissected to validate the imaging results. Tissue samples were excised and histologically analyzed after standard H&E staining.

**Integrated photoacoustic and ultrasonic endoscopic probe.** We designed and implemented a new endoscopic probe for simultaneous photoacoustic and ultrasonic imaging. The new probe has a streamlined shape and is smaller (outer diameter 3.8 mm, 38 mm rigid distal length) than our first-generation probe<sup>30</sup>. To improve the overall image quality, transverse resolution and the signal sensitivity, we fabricated a focused ultrasonic transducer with a piezoelement of single crystal LiNbO<sub>3</sub> (~36 MHz, 65% fractional bandwidth), with a 2.6-mm aperture and a 0.5-mm-diameter central hole to route the optical fiber that delivers laser beams. To equip the probe with the capability of rotational scanning, we incorporated a built-in actuator (**Fig. 1a**) composed of a micromotor (Namiki Precision) and other mechanical components necessary for water sealing (**Supplementary Fig. 1**). We encapsulated the optical fiber, the ultrasonic transducer's signal wires and the actuator's electric wires in a ~1-m-long flexible plastic sheath.

### Dual-wavelength photoacoustic and ultrasonic endoscopic imaging system.

For dual-wavelength photoacoustic imaging, we used two identical pulsed laser systems to generate the first and second laser wavelengths. Each system was composed of a tunable dye laser (Cobra HRR, Sirah) pumped by a solid-state, diode-pumped, neodymium-doped yttrium lithium fluoride laser (INNOSLAB IS811-E, EdgeWave). We used an ultrasonic pulser-receiver (5072 PR, Panametrics-NDT, Olympus), which provided sharp electric pulses to the ultrasonic transducer to generate acoustic pulses for ultrasonic imaging and also amplified the ultrasonic and photoacoustic signals detected by the transducer. More detailed information on the connection of these systems is provided in **Supplementary Figure 1**.

**Data acquisition and processing.** We developed a LabVIEW software (National Instruments)-based data acquisition program that records and displays dual-wavelength photoacoustic and ultrasonic B-scan images in real time (~4 Hz) during the endoscopic imaging procedure. We produced the

volumetric images after doing each animal experiment. In the ultrasonic B-scan images, strong acoustic reflections were generated by the plastic membrane (imaging window) of the probe. The reflected signals identified the boundary of the membrane. We filtered out the multiple reverberation signals generated by the membrane throughout the entire ultrasonic B-scan image. We applied envelope detection to all photoacoustic and ultrasonic A-line data, and time-gain compensation to the extracted amplitude signals. To produce volumetric images of the upper gastrointestinal tract, we used a surface-alignment algorithm and simple spatial filtering, at the expense of image resolution, to reduce the strong motion artifacts primarily caused by periodic respiration. We produced all photoacoustic and ultrasonic images by mapping the signal amplitudes on a linear scale.

**Upper gastrointestinal tract imaging of rabbits.** We imaged the esophagi of adult New Zealand white rabbits ( $n = 4$ , female, ~6 months old, ~4 kg; Myrtle Rabbitry). We anesthetized each rabbit with 35–50 mg kg<sup>-1</sup> of ketamine and 5–10 mg kg<sup>-1</sup> of xylazine (injected intramuscularly). While anesthetized, the rabbit was intubated and supplied with maintenance gas for anesthesia (1.5–3.0% isoflurane). We inserted an endotracheal tube cuff into the trachea and inflated it to prevent aspiration of water into the lung. We placed the rabbit on an inclined stage (~10°) in supine position. Just before probe insertion, we introduced water into the esophagus and stomach by using an enteral feeding syringe connected to a rubber feeding tube (8–12 F). The water provided the necessary acoustic coupling and functioned as a lubricant during the imaging procedure. After filling the stomach and esophagus with water, we inserted the endoscopic probe through the mouth and advanced it ~30 cm into the esophagus, and then immediately initiated endoscopic imaging. Throughout the experiment, we continuously monitored the rabbit's anesthesia level and vital signs. After the experiment, we killed the rabbit by an overdose of pentobarbital (150 mg kg<sup>-1</sup>) injected in the marginal ear vein.

**Lower gastrointestinal tract imaging of rats.** We imaged the colons of adult Sprague-Dawley rats ( $n = 5$ , male, ~5 months old, ~450 g; Harlan National Customer Service Center). In each experiment, we anesthetized the rat with 4% isoflurane for induction, and intraperitoneally administered a cocktail of 87 mg kg<sup>-1</sup> ketamine and 13 mg kg<sup>-1</sup> xylazine to provide time to prepare and mount the animal. After properly positioning the animal, we inserted medical ultrasound gel into the descending colon via a small plastic tube. The ultrasound gel provided acoustic coupling between the tissue and endoscope and lubricated the probe during colon insertion through the anus. During imaging, we maintained anesthesia with 1.5–2.0% isoflurane supplied through a nose cone. After the experiment, we killed the rat by an intraperitoneal pentobarbital overdose (150 mg kg<sup>-1</sup>).